Impact of the Surface Microenvironment on the Redox Properties of a Co-Based Molecular Cathode for Selective Aqueous Electrochemical CO2-to-CO Reduction

Matthieu Haake, Dmitry Aldakov, Julien Pérard, Giulia Veronesi, Antonio Aguilar-Tapia, Bertrand Reuillard, Vincent Artero

Impact of the surface microenvironment on the redox properties of a Co-based molecular cathode for selective aqueous electrochemical CO_2-to-CO reduction

Matthieu Haake,[1] Dmitry Aldakov,[2] Julien Pérard,[1] Giulia Veronesi,[1] Antonio Aguilar Tapia,[3] Bertrand Reuillard[1]* and Vincent Artero[1]

[1] Univ. Grenoble Alpes, CNRS, CEA, IRIG, Laboratoire de Chimie et Biologie des Métaux, 17 rue des Martyrs, F-38054 Grenoble cedex, France

[2] Univ. Grenoble Alpes, CNRS, CEA, Grenoble INP, IRIG, SyMMES, 38000 Grenoble, France

[3] Institut de Chimie Moléculaire de Grenoble, UAR2607 CNRS Université Grenoble Alpes, Grenoble F-38000 (France)

Abstract: Electrode-confined molecular catalysts are promising systems to enable efficient conversion of CO_2 to useful products. Here, we describe the development of an original molecular cathode for CO_2 reduction to CO, based on the non-covalent integration of a tetraazamacrocyclic Co complex to a carbon nanotube (CNT) based matrix. Aqueous electrochemical characterization of the modified electrode allow to clearly observe a change of redox behavior of the Co center as surface concentration was tuned, highlighting the impact of the catalyst microenvironment on its redox properties. The molecular cathode enabled efficient CO_2-to-CO conversion in fully aqueous conditions giving rise to turnover number (TON_{CO}) up to 2 x 10^4 after 2 hours of constant electrolysis at mild overpotential (η = 450 mV) and with faradaic efficiency for CO of about 95%. No obvious degradation of the catalyst could be observed *post operando* using electrochemical techniques, ICP, XPS and XAS characterization of the films making this Co-based electrode a new promising alternative for molecular electrocatalytic conversion of CO_2 to CO in fully aqueous media.

Introduction

The aim to mitigate the impact of global warming requires a drastic decrease in our fossil fuels uses along with implementation of strategies allowing the closing of the carbon cycle.[1–3] To achieve the latter target, efficient electrocatalytic systems need to be developed and integrated within functional electrolyzer devices to allow the mass scale conversion of CO_2 waste to useful compounds using renewable electricity as main energy input.[4–6] The electrocatalytic reduction of CO_2 (CO_2RR) can trigger the production of a variety of more of less complex compounds with specific industrial applications, from the simple C_1 products CO and formate to more electrons-rich ones such as methane, methanol or C_{2+} such as ethylene or ethanol.[4,7] Recent developments in metal-based electrode material, mostly Cu-based,[8–10] have enabled the production of higher added-value products such as ethylene,[11–13] methane[14–16] or ethanol.[17] However, while these processes have been largely improved over the past 5 years, the complexity of the successive reduction steps still leads to mixtures of products which limit the maturity of these systems.[8–10] On the other hand CO, the simplest of all CO_2 reduction products, is a pivotal building block in the chemical industry ranging from the production of hydrocarbons through the use of Syngas mixtures in Fischer-Tropsch processes or methanol production[18,19] to carbonylation of alkenes (hydroformylation) and alkyl/aryl halides and alcohols.[20] Recent work have also studied the direct electrocatalytic reduction of CO (CORR)[21] to more electrons and protons- rich products using mostly Cu-based catalysts.[22,23] Consequently, tandem catalytic systems have emerged to first

selectively reduce CO_2 to CO which is in turn reduced to generate C_{2+} products with better selectivity and efficiencies.[24,25] Recent projections have also showed that electrochemical CO production is close to be cost competitive, approaching the price of fossil-sourced CO.[26]

Fully molecular approaches have been explored to generate efficient and selective earth-abundant transition metal catalysts for CO_2 reduction, mainly to CO and HCO_2^-.[27–29] The use of synthetic methods allows the fine-tuning of molecular designs, which in turn gives access to structure/activity relationships that can lead to further optimizations of the molecular center in terms of activity, stability, and selectivity. A large body of work has now showed that the catalyst properties could be tuned through structural modifications by simply changing the nature of the ligand,[30–32] its steric/conformational attributes,[33,34] its conjugation and redox activity properties to master electronic density at the metal centre[35–37] or even designing so-called "outer coordination sphere".[38–44]

While these molecular approaches are of major interest to further understand key processes involved in the catalytic mechanisms, such molecular centers require to be hybridized with electrode surfaces in order to shift from basic science to potential applications.[45–47] Over the past ten years, many studies have demonstrated the benefit of anchoring molecular catalysts at electrode surfaces, using covalent or non-covalent grafting methods. Among the most studied grafted earth-abundant metals containing structures for CO_2 reduction, Co, Fe and Ni-based macrocycles have been used extensively[48–55] as well as polypyridine-based metal complexes.[56–60] Integration of such molecular structures to nanomaterials such as carbon nanotubes or combination in metal organic frameworks (MOFs) has enabled the development of highly active hydride electrodes able to deliver current densities in the range of the tens of mA cm^{-2} at reasonable overpotentials and with good selectivity towards CO.[61–65] Recently, integration to flow devices or zero-gap electrolyzers have even shown first functional proof of concept of molecular-based CO_2 electrolysers.[66–69]

In this work, we describe the original derivatization and subsequent electrode immobilization of a cobalt macrocyclic pyridildiimine complex (**CoN_4H**) first studied by the groups of Peters[70] and Frei[71,72] in organic media, revisited by the group of McCrory[37] and recently coupled to a photosensitizer to be integrated within a syngas producing photoelectrochemical cell (Figure 1a).[73] Through the incorporation of a pyrene-anchoring group at the macrocyclic ligand and its subsequent integration to carbon nanotube (CNT) based electrode through non-covalent grafting, the electrocatalytic properties of the grafted Co macrocyclic complex for CO_2 reduction were investigated for the first time in fully aqueous media. The ease of surface functionalization enabled by the non-covalent binding of the pyrene anchor to the CNT sidewalls allowed to conveniently vary the catalyst surface concentration. CA experiments showed that the selectivity towards CO was improved below –0.8 V vs SHE, reaching 95 ± 5% at –1.0 V vs SHE (η = 450 mV). High TON_{CO} up to $20x10^3$ were obtained after 2h electrolysis in CO_2-saturated carbonate electrolyte with no obvious degradation of the Co center.

Results and discussion

*Synthesis and characterization of $[Co^{III}(N_4H\text{-}Ph_{Pyr})Cl_2]Cl$ (**$CoN_4H\text{-}Ph_{Pyr}$**).* The tetraaza-macrocylic Co complex bearing the pyrene anchor was synthesized through a 6-step process starting from chelidamic acid with an 18% overall yield (Figure S1). Following the chlorination of the pyridine moiety in *para* position and the formation of the acetyl groups, the resulting diacetyl pyridine was further modified using a Pd-catalysed Suzuki-Miyaura cross-coupling in order to implement a protected carboxylic acid group allowing for further derivatization of the ligand. Templated macrocyclization was performed using $CoCl_2$, 3,3'-diaminodipropylamine and the diacetyl pyridine intermediate under microwave conditions to yield the Co macrocycle **5**. Following deprotection of the carboxylic acid group with

trifluoroacetic acid (TFA), **CoN_4H-Ph_{Pyr}** (Figure 1a) was obtained through the coupling of a pyrene butylamine with a free carboxylic acid residue using hexafluorophosphate azabenzotriazole tetramethyl uronium (HATU). The final compound was fully characterized using NMR, IR, UV-vis spectroscopies and high-resolution mass spectrometry (Figure S2-4). A parent compound lacking the pyrene-anchoring unit at the end of the butyl chain, **CoN_4H-Ph_{Bu}**, was synthesized using the same methodology, in order to probe the impact of the macrocycle substitution on the electrochemical and electrocatalytic properties of the Co center.

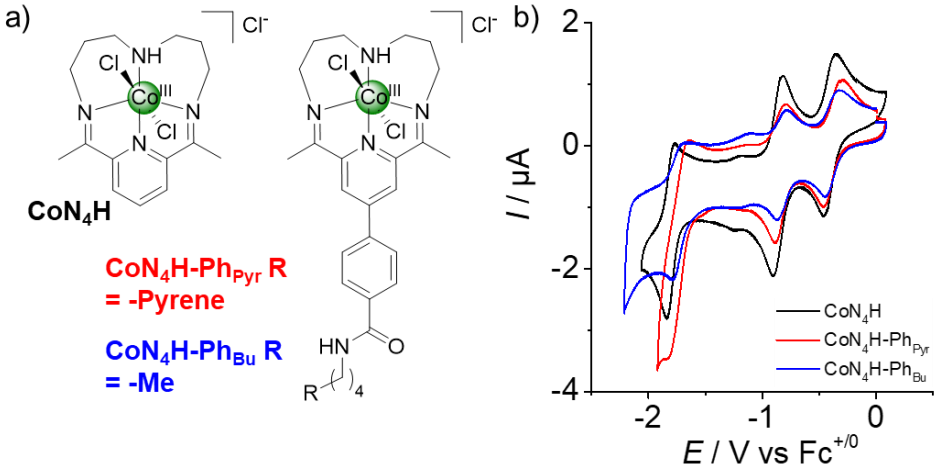

*Figure 1: a) Structures of **CoN_4H** parent complex and its pyrene-modified counterpart **CoN_4H-Ph_{Pyr}** and **CoN_4H-Ph_{Bu}** ; b) CVs of **CoN_4H** (black trace), **CoN_4H-Ph_{Pyr}** (red trace) and **CoN_4H-Ph_{Bu}** at 1 mM in MeCN, 0.1 M $TBAPF_6$ under argon (v = 100 mV s^{-1}).*

Homogeneous electrochemical characterization. The electrochemical properties of **CoN_4H-Ph_{Pyr}** and **CoN_4H-Ph_{Bu}** were first studied and compared with the parent **CoN_4H** complex. CVs performed in MeCN 0.1 M $TBAPF_6$ showed very similar electrochemical behavior between the three compounds, as expected, with a slight anodic shift observed for all redox events for **CoN_4H-Ph_{Pyr}** and **CoN_4H-Ph_{Bu}** (Figure 1b, Table S2). This shift can be explained by the electronic coupling stemming from the phenyl group in *para* position of the pyridine ligand which pulls the electronic density away from both the Co center and the electroactive pyridyl diimine moiety, as previously demonstrated by McCrory and coworkers.[37] For **CoN_4H-Ph_{Pyr}**, a first reversible redox process corresponding to the $Co^{III/II}$ redox couple is observed at $E_{1/2}$ = –0.38 V vs $Fc^{+/0}$ with a 0.03 V anodic shift compared with the parent **CoN_4H** complex. Another reversible process attributed to the $Co^{II/I}$ redox couple was observed at $E_{1/2}$ = –0.83 V vs $Fc^{+/0}$, 0.03 V more anodic than with the parent compound. Finally, the redox process expected from the pyridyl diimine moiety is observed with a partially reversible redox process at $E_{1/2}$ = –1.74 V vs $Fc^{+/0}$ and with a more pronounced anodic shift of 0.07 V compared to the **CoN_4H** reference. A small redox event for all complexes could be spotted between –1.21 and –1.14 V vs $Fc^{+/0}$ which could not be attributed with certainty. The electrocatalytic behavior of the newly synthesized complexes towards the reduction of CO_2 was also characterized in organic media and compared to the parent complex (Figure S5 and S6). First, CVs obtained following the addition of 11 M of H_2O as proton source showed the appearance of a catalytic wave, likely attributed to the reduction of protons by the Co center as previously reported (Figure S5).[37] After saturation of the electrolyte with CO_2, a clear catalytic wave could be observed at $E_{cat/2}$ = –1.75, –1.70 and –1.66 V vs $Fc^{+/0}$ for **CoN_4H**, **CoN_4H-Ph_{Pyr}** and **CoN_4H-Ph_{Bu}**, respectively. In order to verify the nature of the catalytic process, controlled potential electrolysis (CPE) measurements were performed for all three complexes at a larger glassy carbon disk, in the presence of the proton source and CO_2, at –1.92 V vs $Fc^{+/0}$ (Figure S6). Stable currents between –1 and –1.5 mA were observed and the produced gases were quantified using gas chromatography. After 1h CPE, 8.2 µmol of CO and 0.3 µmol of H_2 were measured for **CoN_4H** with a faradaic efficiency for CO (FE_{CO}) of

69%. For **CoN_4H-Ph_{Pyr}**, 6.8 µmol of CO and 1.0 µmol of H_2 were measured with a comparable FE_{CO} of 65% while **CoN_4H-Ph_{Bu}** allowed the production of 5.0 µmol of CO and 2.5 µmol of H_2 with a slightly lower FE_{CO} of 54% (only traces of formate were detected in the electrolyte post-CPE, in same quantity as for the blank electrolysis without catalyst, suggesting that formate production stemmed from DMF hydrolysis) (Table S2). Thus, the FE_{CO} obtained with **CoN_4H-Ph_{Pyr}** and **CoN_4H-Ph_{Bu}** are comparable to the recently reported work by Nie et al. for the phenyl-derived complex, although we found a higher selectivity for CO with the parent complex **CoN_4H,** which could arise from the change in electrolyte.[37] CPE performed at –2.20 V vs $Fc^{+/0}$ with **CoN_4H-Ph_{Pyr}** highlighted that the second wave observed can mainly be ascribed to proton reduction as FE_{CO} drops from 65 to 45% while FE_{H2} rise from 10 to 32% (Figure S6). The relatively low overall FE, close to the one observed in previous work,[37] can potentially be attributed to partial reduction and/or degradation of the molecular unit in these conditions.

Electrode integration and heterogeneous electrochemical characterization. The MWCNT electrodes were prepared by drop-casting of a MWCNT dispersion in ethanol (3 mg mL^{-1}), allowing to obtain a homogeneous thick and porous network of MWCNT at the surface of the GC electrode (Figure S7). The MWCNT electrodes were then let to dry before being soaked in 5 mM solution of **CoN_4H-Ph_{Pyr}** in DMF and then washed successively with DMF and deionized water. The presence of the pyrene anchor allowed for smooth and simple integration of **CoN_4H-Ph_{Pyr}** at the surface of multiwalled carbon nanotube (MWCNT) modified glassy carbon (GC) electrode through π-π interactions between the pyrene and the π-conjugated CNT sidewalls (Figure 2a). The electrochemical characterization of the **CoN_4H-Ph_{Pyr}**|MWCNT-modified electrodes were then performed in aqueous potassium bicarbonate electrolyte (0.5 M) (Figure 2b).

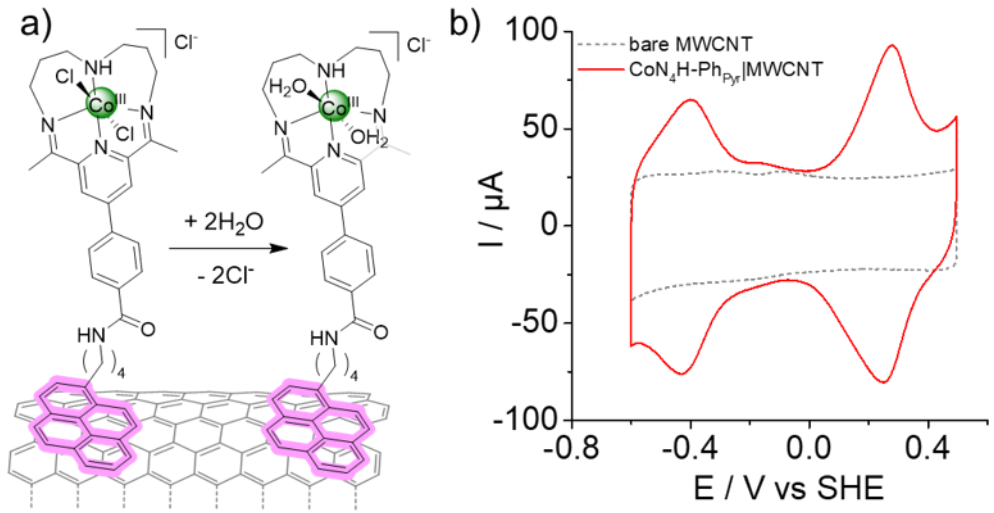

*Figure 2: a) Schematic representation of the **CoN_4H-Ph_{Pyr}**|MWCNT electrode assembly and proposed displacement of the Cl^- ligands by H_2O as observed using XAS spectroscopy; b) CV measurements of the **CoN_4H-Ph_{Pyr}**|MWCNT-modified electrode (red trace) and of a bare MWCNT|GC (grey dashed trace) in 0.5 M $KHCO_3$, under N_2 atmosphere (v = 20 mV s^{-1})*

CV measurements were carried out and could show very distinct reversible redox signals at $E_{1/2}$ = 0.26 and –0.40 V vs SHE that likely correspond to the $Co^{III/II}$ and $Co^{II/I}$ redox processes, respectively (Figure 2b). As expected for an immobilized species, both the anodic and cathodic peak current increased linearly with the scan rate, up to 0.5 V s^{-1} (Figure S8). The lower peak current values observed at higher scan rates (> 0.5 V s^{-1}) can most likely be explained by mass transport limitation within the MWCNTs network, as commonly observed for porous films.[74,75] The solution structure of the Co center at the working electrode was probed with Co K-edge X-ray Absorption Spectroscopy (XAS). In the solid state, Co in the catalyst is in octahedral coordination, bound to four N/O atoms at 1.96 ± 0.03 Å and two Cl atoms at 2.24 ± 0.02 Å as planar and axial ligands, respectively (the details of the analysis and cell setup

are reported in the SI and Figure S9). Upon immersion of the **CoN$_4$H-Ph$_{Pyr}$** modified electrode in the aqueous electrolyte, both the X-ray Absorption Near-Edge Structure (XANES, Figure S10a) and the Extended X-ray Absorption Fine Structure (EXAFS, Figure S10b) regions of the spectra highlight the absence of Cl^- ligands, and suggest that Co is bound only to N/O ligands, in octahedral coordination. These evidences confirm the findings reported by Moonshiram et al,[76] concerning the substitution of the axial Cl with aqua ligands in a macrocyclic Co catalyst in solution. Thus, the initial species present at the surface of the electrode when electrochemistry is performed is a bis-aqua complex (Figure 2a).

As mentioned above, this simple non-covalent immobilization process usually allows to efficiently control the surface loading of the grafted molecular entity by simply changing the concentration of the catalyst in the incubation solution. This electrode preparation strategy differ from the widely employed ink deposition where a mixture of catalyst and carbon support is directly deposited at the conducting support[77–79] and has the advantage to prevent aggregation to maximize the amount of electroactive species.[69] Thus, a range of concentrations (from 0.5 to 20 mM) of the soaking solution of **CoN$_4$H-Ph$_{Pyr}$** used for the electrode functionalization was screened (Figure 3).

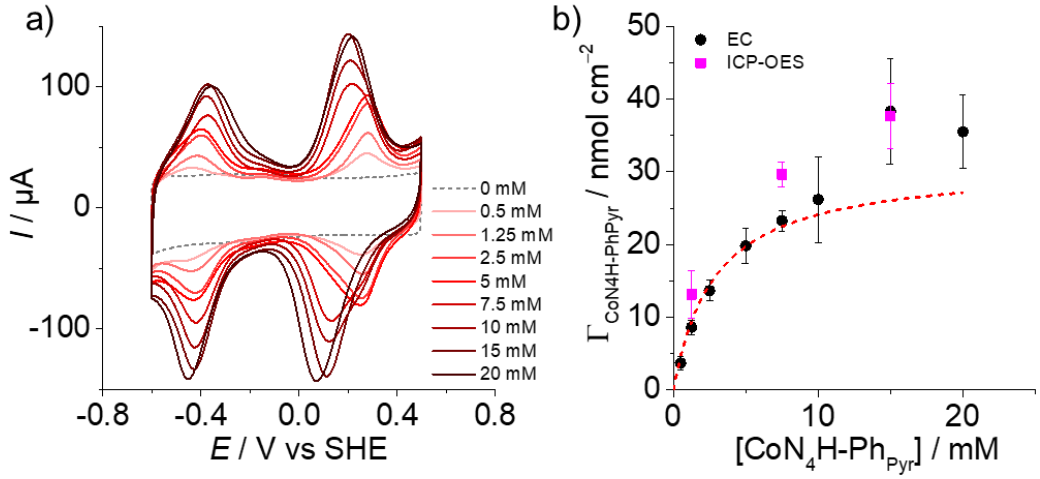

*Figure 3: a) CV of the **CoN$_4$H-Ph$_{Pyr}$**|MWCNT|GC electrode modified in increasing concentration of the soaking solution in 0.5 M $KHCO_3$ under N_2 (v = 20 mV s^{-1}); b) Evolution of the surface concentration of **CoN$_4$H-Ph$_{Pyr}$** as function of the concentration of the soaking solution measured electrochemically (EC, black dots) or using ICP-OES (purple squares). The red dashed trace represents the best isotherm fitting of the EC data points.*

As expected, the redox responses of both the $Co^{III/II}$ and $Co^{II/I}$ redox signals became more intense as the concentration of **CoN$_4$H-Ph$_{Pyr}$** in the soaking solution increased (Figure 3a). This shows that the surface loading of the complex indeed logically evolves when the soaking concentration is changed, as the equilibrium for adsorption is modified. The surface concentrations of the grafted and electrochemically responsive Co center ($\Gamma_{CoN4H\text{-}PhPyr}$) could be obtained through the integration of the oxidation wave of the $Co^{III/II}$ redox process. Surface loadings ranging from 4 ± 1 to 38 ± 7 nmol cm^{-2} could be measured at concentrations of 0.5 and 15 mM, respectively, in the same range as for other pyrene-modified catalysts deposited on similar MWCNT-based electrodes.[58,80] The evolution of the Co loading with the soaking concentration of the complex could be fitted using a simple Langmuir isotherm (Figure 3b, see SI for details). The best fit was obtained with a saturating surface concentration ($\Gamma_{Co.\ max}$) of 31 nmol cm^{-2} to give an association constant of 350 M^{-1}, slightly lower than previously reported K values for the adsorption of pyrene-modified coordination complexes at MWCNT electrode surfaces.[58,80] Surface saturation thus seems to be reached at soaking concentrations between 7.5 and 10 mM, above these values the catalyst is likely to be deposited inhomogeneously and to form aggregates. For all the soaking concentrations probed, the peak current responses as a function of the scan rate remained linear, again, up to 0.5 V s^{-1} (Figure S11-S17). In parallel, inductively coupled plasma optical emission

spectroscopy (ICP-OES) allowed to further quantify the total amount of Co contained in the MWCNT films. Slightly higher Co loadings were measured, indicating that between 21 and 34% of the catalyst remained electrochemically silent after soaking the electrode in 7.5 and 1.25 mM solutions of **CoN_4H-Ph_{Pyr}**, while at larger concentrations, similar surface loadings were measured for both electrochemical and ICP-OES measurements (Table S3).[75] Poor electrochemical wiring could simply explain this discrepancy although recent work also hinted that direct electronic coupling between the adsorbed molecule and the surface, more likely at low catalyst loadings, could also lead to the absence of redox response.[81] The larger discrepancy observed between the EC and ICP-based surface loadings at lower surface concentration could be explained by a less dense layer of catalyst which could allow for facilitated electronic coupling between the conjugated domain of **CoN_4H-Ph_{Pyr}** and the MWCNT electrode surface as recently proposed.[81] Such coupling would be less likely in the case of a densely packed catalyst layer.

Another obvious feature observed when increasing the surface loading is the shift in redox potentials of both the $Co^{III/II}$ and $Co^{II/I}$ redox processes (Figure 3a and S18, Table S3). For the $Co^{III/II}$ redox couple a very sharp shift in potential is observed when going from surface concentration below 20 nmol cm^{-2} to higher surface loadings (Figure S18a). Below $\Gamma_{CoN4H\text{-}PhPyr}$ = 20 nmol cm^{-2}, the $E_{1/2}$ of the $Co^{III/II}$ redox couple sits at $E_{1/2}$ = 0.26 V vs SHE and drops to $E_{1/2}$ = 0.16 V vs SHE at increasing surface coverage above 20 nmol cm^{-2}. At intermediate surface concentrations (obtained with soaking concentration of between 5 and 10 mM), broader redox responses can be observed where the contribution of the two redox events probably overlap (Figure S18a and c). In parallel, the $Co^{II/I}$ redox couple shifts linearly when increasing the surface loading, from $E_{1/2}$ = –0.45 to –0.40 V vs SHE, until reaching 20 nmol cm^{-2} when the redox potential then stabilizes even at higher loadings (Figure S18b and d). Interestingly, the sharp potential shift of the $Co^{III/II}$ redox process occurs at the surface concentration when the MWCNT electrode surface seems to saturate, around $\Gamma_{CoN4H\text{-}PhPyr}$ = 20 nmol cm^{-2}, according to the Langmuir plot (Figure 3b, S18c). Similarly, the stabilization of the $Co^{II/I}$ redox potential also occurs at loadings above 20 nmol cm^{-2} (Figure 3b and S18d). These changes in redox activity occurring when varying the surface concentrations can most probably be attributed to a change in organization of the Co centers at the surface of the electrode and potentially to intermolecular interactions as site density increases. From the scan rate dependency studies of the peak currents performed for each modified electrodes (Figure S8 and S11-S17), peak separation was extracted and plotted as function of the log of the scan rate in order to perform a Laviron analysis[82,83] of the **CoN_4H-Ph_{Pyr}**|MWCNT electrodes with various surface loadings (Figure S19). From these plots, electrons transfer rate (k_{ET}, see SI for detailed calculation) could be calculated. Interestingly, it appears that at lower surface loadings (< 20 nmol cm^{-2}) k_{ET} are situated between 2.5 and 4.5 s^{-1} while at higher loadings (> 20 nmol cm^{-2}) the k_{ET} drop to below 1 s^{-1} (Figure S20). The latter values corresponds to the rate measured in a recent study for a parent complex bearing a similar but shorter linker.[84] This decrease in ET rates could potentially hint towards reorganization occurring at higher loading, potentially whilst monolayer formation, increasing the distance between the Co center and the MWCNT surface (although distorted signal, e.g. large peak-to-peak separation, could also stem from the electrolyte mass transport limitations in the porous electrode when large current response are observed). This phenomenon has previously been described for other adsorbed/grafted redox active compounds. For instance, the group of Dempsey showed that the redox activity of ferrocene could be affected by the interaction between the redox sites at an electrode surface.[85] In addition, lateral interactions between redox and non-redox active species in self-assembled monolayers have previously been described to strongly impact redox properties of the absorbed redox probe.[86–88] More work, including surface co-immobilization of the Co centers with other surface functions as diluent, needs to be performed in order to fully understand the observed redox behavior and how the microenvironment around the metal center can influence its

redox response as well as its catalytic properties. These results underline the potential interest of such fine control over surface loading in order to control the local organization and tune the microenvironment of a grafted catalyst.

Electrocatalytic performances of the ***CoN$_4$H-Ph$_{Pyr}$****|MWCNT cathode.* Following these electrochemical characterizations, the **CoN$_4$H-Ph$_{Pyr}$**|MWCNT-modified electrodes were then tested for their ability to electrocatalytically reduce CO_2 in fully aqueous media. Electrodes prepared with 7.5 mM soaking solution of Co complex were first studied as they allow, according to the Langmuir plot above, saturating the electrode surface with Co centers.

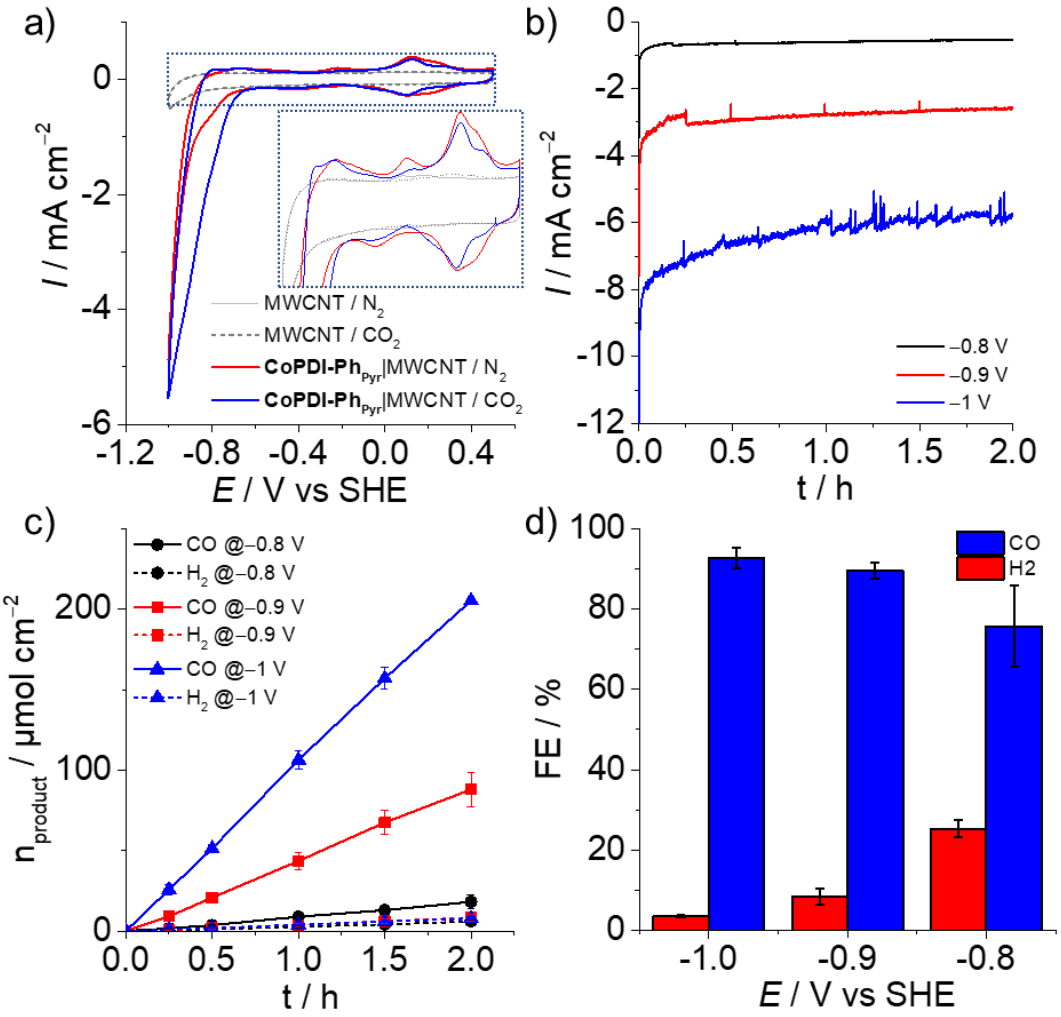

Figure 4: Electrochemical and electrocatalytic characterisation of the ***CoN$_4$H-Ph$_{Pyr}$****|MWCNT electrode modified with 7.5 mM of Co complex in the soaking solution. a) CV performed under N_2 (red trace, 2nd scan showed) and in CO_2-saturated electrolyte (blue trace, 4th scan showed following measurements under N_2), blank MWCNT|GC electrode under N_2 (light grey full trace) and in CO_2-saturated electrolyte (grey dashed trace) (v = 20 mV s^{-1}). Inset: zoom on the non-catalytic redox responses of the* ***CoN$_4$H-Ph$_{Pyr}$****|MWCNT electrode ; b) CA performed at –0.8 vs SHE (black line), –0.9 (red line) and –1.0 V vs SHE (blue line); c) Amount of CO (full lines) and H_2 (dashed lines) produced over time at –0.8 (black dots), –0.9 (red squares), and –1.0 V vs SHE (blue triangles); d) Faradaic efficiencies for CO (blue columns) and H_2 (red columns) as a function of the applied potential after 2h of CPE. All experiments were performed in 0.5 M $KHCO_3$ degassed with either N_2 (pH 8.6) or CO_2 (pH 7.4)*

CVs performed in 0.5 M $KHCO_3$ electrolyte (pH 8.6) under an N_2 atmosphere scanning towards more negative potentials showcase distinctly different features than those observed above (Figure 4a). First, a large irreversible wave reaching about –4.9 mA cm^{-2} is observed, starting at around E_{onset} = –0.75 V vs SHE, which is likely to be stemming from proton reduction as previously reported for a similar Co catalyst (see below for details). In addition, the previously observed redox features of the Co$^{III/II}$ and

$Co^{II/I}$ couples are drastically modified upon further reducing the Co center, most likely below its Co^{I} state (Figure S21). First, following the further reduction of the Co^{I}, the $Co^{II/I}$ couple loses its reversibility and a new oxidation peak is instead observed at $E_{ox.}$ = –0.19 V vs SHE, which could be attributed to the formation of the Co^{II} specie (Figure S21a, inset). Following successive scans in the catalytic wave region a very obvious shift of the $Co^{III/II}$ redox couple can be noticed, shifting towards more negative potentials (from $E_{1/2}$ = 0.16 to 0.04 V vs SHE) (Figure 4a, inset and Figure S21b, inset). Concomitantly, the initial $Co^{II/I}$ redox process disappears while a new oxidation peak can be observed at $E_{ox.}$ = –0.68 V vs SHE on the backward roughly at the same potential that of the catalytic wave. These observations clearly hint towards changes in the direct environment of the Co centers upon reduction below the Co^{I} state. In the CO_2-saturated electrolyte (pH = 7.4), a catalytic wave is observed at E_{onset} = –0.65 V vs SHE, therefore positively shifted by 100 mV compared to the one obtained under N_2 atmosphere. This corresponds to a larger potential shift than what would be expected if only the pH had been modified, suggesting that an additional reactivity could stem from this catalytic process. This catalytic wave could then be assigned to CO_2 reduction to CO (see below) which is thus initiated at low overpotential of about 100 mV ($E^0_{CO2/CO}$ = –0.55 V vs SHE at pH 7.4).

In order to gain further insight on the stability of the observed catalytic process, chronoamperometry measurements (CA) were performed at three different potentials using a typical 2-compartment H-cell setup (Figure 4b, S22 and S23). Production of gaseous substrates, namely CO and H_2, was also monitored using gas chromatography (GC) (Figure 4c and d). As expected from previous CV measurements, catalytic currents ramped up when the applied overpotential was increased from η = 250 to 450 mV. After 5 min of CA measurements, current densities of about –0.8 ± 0.1, –3.1 ± 0.4 and –6.9 ± 0.7 mA cm^{-2} were measured at applied potentials of –0.8, –0.9 and –1.0 V vs SHE, respectively (Table S4). Between 70% (at –0.8 V) and 80% (at –1.0 V) of current was retained following 2 hours of CA, indicating a relative stability of the modified electrodes even at more negative applied potentials. The higher current densities obtained at larger overpotential translated into an increased production of CO with 205 ± 2 µmol cm^{-2} after 2 hours CA at –1.0 V vs SHE, compared to 18 ± 5 µmol cm^{-2} and 88 ± 11 µmol cm^{-2} at –0.8 and –0.9 V vs SHE, respectively (Figure 4c). At all potentials, steady production of gas could be quantified over time with a net increase of selectivity towards the electroproduction of CO compared to H_2 at higher applied overpotential starting from 76 ± 10% at –0.8 V vs SHE and reaching 93 ± 3% at –1.0 V vs SHE (Figure 4c and d). Therefore, a non-negligible improvement in FE_{CO}, from 65 to above 90%, is observed following the grafting of the Co center and shifting from organic to aqueous electrolyte and this has has been previously observed in molecular catalysis for CO_2 reduction.[53,77,89,90] These changes of selectivity can be attributed to a change of reactivity of some key intermediates in a different solvent (e.g. change in hydricity)[91] but also to the drastic change in local environment stemming from surface integration.[92] At a carbon surface, electronic coupling,[77,93,94] solvation,[81] hydrophobicity/hydrophilicity and the local pH[95] during catalysis vary significantly compare to homogeneous conditions and as function of the choice of electrolyte. In addition, the change of selectivity observed when going from low to high applied overpotential could arise from a change in local pH when current densities rise, leading to fast proton consumption and thus to more alkaline conditions at the electrode surface.

As expected, control experiments performed with a non-modified MWCNT electrode only allowed to observe very small current density and negligible CO and H_2 production while the presence of a Co salt ($CoCl_2$) in the electrolyte only slightly increased the production of CO (Figure S24). CA measurements with the parent Co complex lacking the pyrene anchor **CoN_4H** showed very similar selectivity as the pyrene bearing counterpart (FE_{CO} > 90%, Figure S24c and d), as expected from homogeneous study, with however much lower current densities (–0.89 mA cm^{-2} after 2h) leading to much lower CO production (39 µmol cm^{-2}) (Figure S24b). Such difference can be explained by a much lower affinity

between the parent **CoN_4H** complex and the MWCNT surface, leading to lower surface loading and to a slow release in aqueous electrolyte overtime, as well as potentially by a more sluggish electron transfer as the larger peak separation is observed for **CoN_4H**|MWCNT (Figure S24a). Without saturation of the aqueous carbonate electrolyte with CO_2, lower and less stable currents are obtained with **CoN_4H-Ph_{Pyr}**|MWCNT (≈ 2 mA cm^{-2}) and low FE_{CO} of 15% most likely stemming from the reduction of the low amount of CO_2 present in the carbonate electrolyte (from $KHCO_3/CO_2$ equilibrium) indicating that CO_2 is the source of CO and that carbonate is unlikely to be directly reduced to CO (Figure S24d).

The higher current densities and FE_{CO} obtained at higher applied overpotential correspond to high specific TON_{CO} above 9 x 10^3 at 450 mV overpotential and to TOF_{CO} of 1.3 ± 0.1 s^{-1} after 2 hours of CA at –1.0 V vs SHE (Figure S25a). When using ICP-OES derived Co loadings, lower TON_{CO} (≈ 7 x 10^3) and TOF_{CO} (1.0 ± 0.1 s^{-1}) are obtained due to the slightly higher Co content measured with this technique (Figure S25b, Table S4). These two sets of data thus give lower and higher estimates of the catalyst activity, comparing more than favorably with the existing literature on immobilized molecular complexes performing in aqueous media at low (450 mV in this work) overpotential.[47] Interestingly, similar metrics for parents Co compounds have been concomitantly obtained by Andrin et al.[96]

*Post operando characterization of the **CoN_4H-Ph_{Pyr}**|MWCNT cathode.* Post-CA experiments CVs were then performed in order to probe the evolution of the redox and electrocatalytic responses of the grafted Co catalyst (Figure 5).

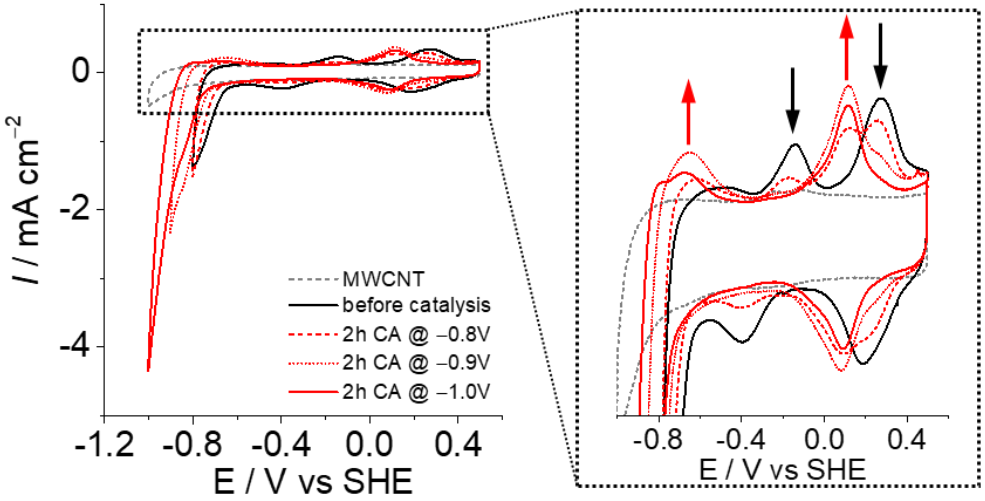

*Figure 5: CVs traces of the **CoN_4H-Ph_{Pyr}**|MWCNT electrode modified with 7.5 mM of Co complex in the soaking solution before (black dashed line) and after 2h CA at –0.8 (red line), –0.9 (purple line), and –1.0 V vs SHE (blue line) in 0.5 M KHCO3 saturated with CO_2 (pH 7.4) (v = 20 mV s^{-1}). The red and black arrows indicate the appearance and disappearance of redox signals, respectively.*

As discussed above, a new reversible redox feature at $E_{1/2}$ = 0.08 V vs SHE (shifting with the pH following CO_2 saturation of the electrolyte) is generated following the poising of the electrode at negative potential and is concomitant with the disappearance of the original $Co^{III/II}$ redox signal at $E_{1/2}$ = 0.21 V vs SHE observed under CO_2 atmosphere (Figure 5). As observed above under N_2 atmosphere, the rise of an irreversible anodic peak can also be spotted at E_{ox} = –0.63 V vs SHE, tentatively be attributed to the $Co^{II/I}$ redox couple oxidation process of the newly generated molecular specie. Successive 1h CA experiments were performed at –0.8, –0.9 and –1.0 V vs SHE to probe the impact of the applied potential on the change in redox properties of the **CoN_4H-Ph_{Pyr}**|MWCNT electrode (Figure S26 and S27). CVs measured before and after sequential CA at different applied potential at which catalysis is effective showcase that the change in redox response occurs slowly at –0.8 V vs SHE and faster when more negative potential are applied (Figure S26). The same change in redox behavior can be followed

using CV, as presented above under N_2 atmosphere, with however a slower formation rate in CO_2-saturated electrolyte (Figure S28). At all applied potentials, the catalytic response remained reasonably stable over the cycles with between 65 and 75% of current retention after four rounds of 1h CA at –1.0 and –0.8 V vs SHE, respectively (Figure S27a, b and c) while the production of CO and the FE_{CO} remained rather stable over time (Figure S27d, e and f). Importantly, the TOF_{CO} only moderately decayed over time at all potentials during the time of the experiments, suggesting no or only slow degradation of the active catalyst in these conditions (Figure S29). After 4h, 95, 92 and 88% of maximum TOFs are retained at –0.8, –0.9, and –1.0 V vs SHE, thus strongly suggesting that the new redox feature belongs to the active catalyst (Figure S29b). In addition, CA experiments performed at –0.8 V vs SHE with the newly generated species (from CA at –1.0 V vs SHE) could confirm that the change in selectivity obtained at the various applied potential is not inherent to the formation of the new complex but rather to the local conditions at the electrode as proposed above (Figure S30).

We note that the intensity of the redox response also tends to slowly decay over time and, assuming a similar monoelectronic process $Co^{III/II}$ (at $E_{1/2}$ = 0.08 V vs SHE), only about 50% of the initial Co electrochemically estimated loading is found after 4h CA at –1.0 V vs SHE (62% after 2h CA, Table S5). This could be the sign of either catalyst degradation or desorption, although this latter hypothesis appears less likely as we recently demonstrated the very stable anchorage of pyrene anchors at the surface of MWCNT-based electrodes.[97] Quantification of the remaining amount of Co in the film at the end of the 2 hours electrolysis experiment was also carried out using ICP-OES. After CA at –1.0 V vs SHE, 16 ± 2 nmol cm^{-2} of Co were detected, corresponding to about 52% of the initial Co amount loaded at the electrode (Table S5). ICP-OES performed on the electrolyte allowed to detect the presence of 4 nmol of Co (corresponding to about 14 nmol cm^{-2} of loaded complex, about 46% of the initial Co amount loaded at the electrode) which confirmed Co release over the course of the electrolysis, likely stemming from ligand degradation over the course of time. In parallel, XPS characterization of the film was performed before and after 4h of CA experiments at –1.0 V vs SHE (Figure S31). Both the Co $2p_{3/2}$ clear signal at 780.8 eV and the N 1s one at 399.9 eV display no obvious changes before and after CA. Overall, this indicates that these elements retained their oxidation state and chemical environment suggesting that the complex did not undergo any significant chemical changes after the catalysis and remained coordinated and grafted.

The fingerprint analysis of the XANES spectra recorded before and after CA experiment at –1.0 V *vs* SHE indicates no obvious change in the coordination of the Co center. The spectral features are the same before and after CA, and no shift in the edge position is observed (Fig. S10a, inset), confirming that the Co coordination geometry and oxidation state are unaltered. The comparison of these spectra with the ones relative to Co metal and oxide reference compounds clearly showcase that no such chemical form is present in the probed electrode surface post-CA (Figure S10a).

Taken together, these observations indicate that despite a very clear change in the redox properties of the deposited catalyst, its molecular integrity appears to be retained. Thus, this redox shift most likely arises from a coordination environment change that occurs when reducing the Co center below the Co^{I} state and generating a molecularly active catalyst. As this species seem to be formed faster at larger overpotential and thus higher current densities, its formation probably indicates a change in the ligand sphere, likely to be related to the increasing basicity of the local surface environment during catalysis or, alternatively, reduction of the ligand by a hydride intermediate as faster formation of this specie under HER conditions could suggest (*vide supra*). More work is currently ongoing in order to try to identify the exact nature this new species. Then, the very slight loss of activity with time could then be explained by a prolonged loss of Co as CV, XPS and ICP-OES experiments discussed above would

suggest, pointing toward potential Co decoordination as the main culprit for the slow loss of activity of the **CoN_4H-Ph_{Pyr}**|MWCNT electrode as no adsorbed degradation product seems to be detected.

Study of the impact of the surface loading on the catalytic process. As discussed above, the **CoN_4H-Ph_{Pyr}** surface concentration influences the redox activity of the $Co^{III/II}$ and $Co^{II/I}$ redox couples. Thus, additional CA measurements were performed at low (9 ± 1 nmol cm^{-2}) and high (38 ± 7 nmol cm^{-2}) surface concentration of **CoN_4H-Ph_{Pyr}** in order to probe a potential impact on the electrocatalytic performances of the Co center (Figure 6). In particular, such influence on the selectivity has previously been observed for other molecular catalysts.[58,98]

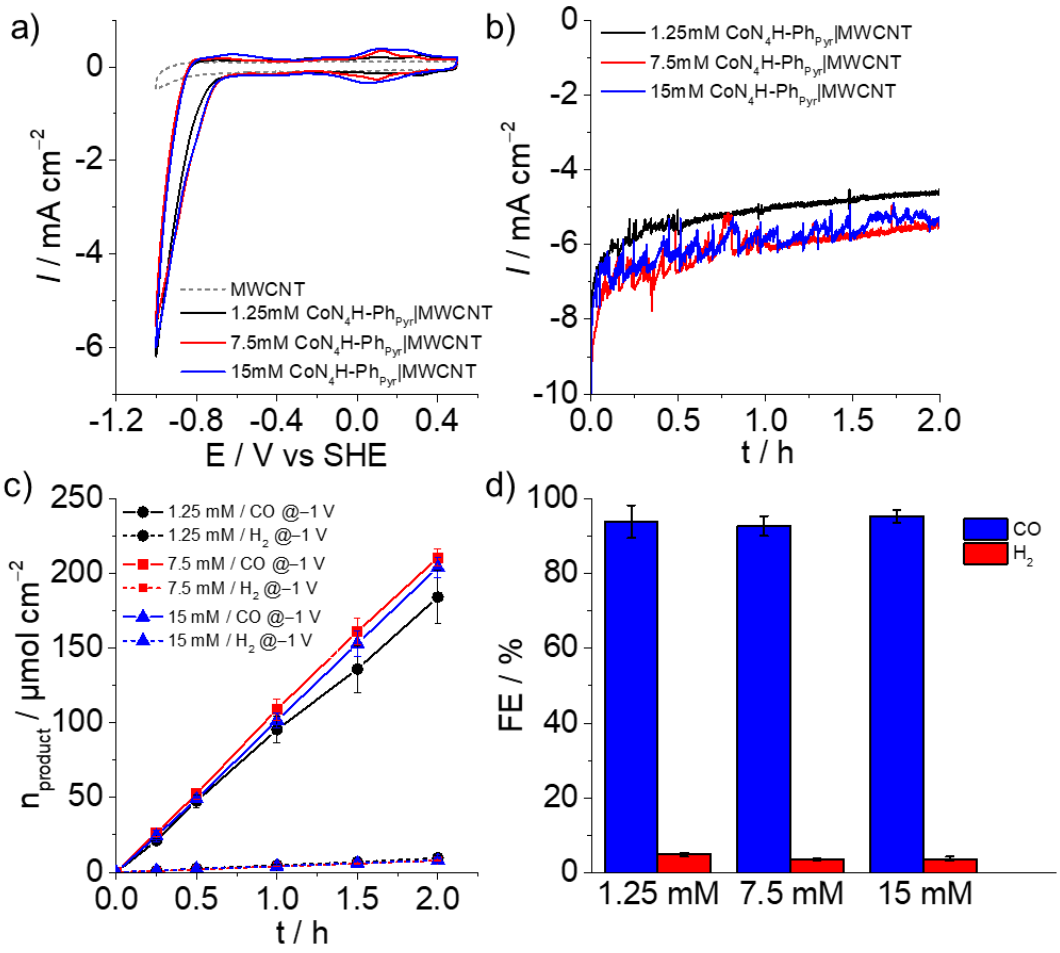

*Figure 6: Electrochemical and electrocatalytic characterization of the **CoN_4H-Ph_{Pyr}**|MWCNT electrode modified with 1.25 (black traces); 7.5 (red traces) and 15 mM (blue traces) of Co complex in the soaking solution. a) CV performed in CO_2-saturated electrolyte in CO_2-saturated electrolyte with MWCNT electrode (grey dashed trace) (v = 20 mV s^{-1}); b) CA performed at –1.0 V vs SHE; c) Amount of CO (full lines) and H_2 (dashed lines) produced over time at –1.0 V vs SHE; d) Faradaic efficiencies for CO (blue columns) and H_2 (red columns) as a function of the Co soaking solution concentration after 2h of CPE. All experiments were performed in 0.5 M $KHCO_3$ degassed with CO_2 (pH 7.4)*

CV performed with the **CoN_4H-Ph_{Pyr}**|MWCNT electrode modified with increasing surface concentrations of Co showed again a drastic difference in the redox response observed depending on the amount of loaded catalyst, attributed to a change in orientation and organization of the Co center at the electrode surface (*vide supra*). In addition, apparition of the new redox process at $E_{1/2}$ = 0.10 V vs SHE (at pH 7.4) is also clearly observed after cycling towards more negative potential values, as observed above. However, the surface concentration had a negligible impact on the catalytic wave in terms of intensity and apparent onset potential (Figure 6a and S32). CA measurements carried out at –1.0 V vs SHE confirmed that only a marginal difference in catalytic response is observed when

increasing the surface concentration of **CoN_4H-Ph_{Pyr}** even after 2h electrolysis (Figure 6b and S33). This lack of influence of the surface concentration onto the catalysis is further corroborated by the product analysis, which shows very similar CO and H_2 production rates and selectivity (FE_{CO} > 93%) at the three concentrations tested (Figure 6c and d). This logically translated in important deviations when calculating the TON_{CO} and TOF_{CO}. At low surface concentration, TON_{CO} as high as 20 x 10^3 (TOF_{CO} ≈ 2.8 s^{-1}) were obtained compared to 5 x 10^3 (TOF_{CO} ≈ 0.7 s^{-1}) at high surface concentration (Figure S34a). Again, slightly more conservative values were obtained when assuming an activity of 100% of the Co measured by ICP-OES (Figure S34b). With such metrics, this **CoN_4H-Ph_{Pyr}**|MWCNT cathode compares well with recently published benchmarks of noble metal-free molecular-based cathode for aqueous CO_2 reduction (Table S6). ICP-OES measurements carried out to quantify the amount of Co left in the film after the CA experiments showed that unexpectedly more Co was retained in the film after 2h at higher catalyst loading (88%) than at low concentration (51%) (Table S5). From EC and ICP loading measurements, there are no clear trends to correlate the amount of lost Co after the electrolysis with the applied potential (and charge passes) or initial amount of Co grafted. Nevertheless, the lack of improvement in current catalytic response with the increase of the Co surface concentration suggests that H^+ and CO_2 availability in the aqueous electrolyte and through the porous film is limiting in these conditions, as previously proposed for Co phthalocyanin modified carbon electrode for CO_2 reduction.[98,99]

Conclusion

In this work, the synthesis and full characterization of an original Co macrocyclic complex modified with a pyrene group, **CoN_4H-Ph_{Pyr}**, was carried out. The presence of such anchoring function enabled the straightforward integration of the macrocycle to MWCNT-modified electrodes. Thorough electrochemical characterization of the modified electrodes allowed observing a changing redox activity dependent on the surface loading, as often observed in SAMs but with however no dramatic impact on the catalytic properties of the grafted catalyst. In a CO_2-saturated electrolyte, the catalytic activity for CO_2 reduction to CO is initiated at an overpotential of only 100 mV. Importantly, shifting from homogeneous organic to heterogeneous aqueous conditions, **CoN_4H-Ph_{Pyr}** showed a largely improved selectivity toward the reduction of CO_2 against the reduction of protons. CA experiments performed at increasing applied overpotential (250, 350 and 450 mV) showed that the activity as well as the selectivity of the **CoN_4H-Ph_{Pyr}** improved at more negative applied voltages, to reach maximum TONs of about 20 x 10^3 after 2 hours of electrolysis with FE_{CO} approaching 95% in the lower catalyst loading range.

These results further underline the benefit of controlled surface integration of molecular catalyst for electrocatalytic small molecule activation and showcase in particular how the catalyst microenvironment can influence its redox properties. Here, incrementing the surface loading did not allow to improve the performance of the modified electrode to produce more CO, hinting that the local concentration of H^+ and CO_2 within the film is probably the limiting factor in the studied condition, as previously proposed for other molecular cathodes for CO_2 reduction. Nevertheless, the properties of the **CoN_4H-Ph_{Pyr}**|MWCNT modified electrode compare very favorably with previously described earth-abundant based cathodes for CO_2 reduction in aqueous conditions.[47]

In future work, this catalyst will be characterized in membrane electrode assembly and integrated within electrolyzer to further test its properties in under non-limiting conditions. Further work will be carried out also to better understand the nature of the newly formed active specie as well as of the interactions responsible for the change of redox behavior of the Co center and in an attempt to take advantage from these to tune the catalyst activity.

Acknowledgements

This work was supported by the French National Agency for Research (Labex ARCANE, CBH-EUR-GS, ANR-17-EURE-0003, ANR-21-CE50-0004). We acknowledge the European Synchrotron Radiation Facility (ESRF) for provision of synchrotron radiation facilities under proposal number CH-6609. Dr. Jacques Pecaut (CEA/DRF/IRIG/DIESE/SyMMES) and Dr. Pierre-Alain Bayle (CEA/DRF/IRIG/DEPHY/MEM) are acknowledged for the ESI-MS and the 400 MHz NMR measurements, respectively.

Author information

Corresponding Author

*Bertrand Reuillard, bertrand.reuillard@cea.fr

Author Contributions

The manuscript was written through contributions of all authors. All authors have given approval to the final version of the manuscript.

Associated content

Supporting Information. The following files are available free of charge. Detailed synthetic procedures, additional electrochemical, spectroscopy data and cell setup configuration (PDF).

References:

(1) Hepburn, C.; Adlen, E.; Beddington, J.; Carter, E. A.; Fuss, S.; Dowell, N. M.; Minx, J. C.; Smith, P.; Williams, C. K. The Technological and Economic Prospects for CO 2 Utilization and Removal. *Nature* **2019**, *575* (7781), 87–97. https://doi.org/10.1038/s41586-019-1681-6.

(2) Grim, R. G.; Huang, Z.; Guarnieri, M. T.; Ferrell, J. R.; Tao, L.; Schaidle, J. A. Transforming the Carbon Economy: Challenges and Opportunities in the Convergence of Low-Cost Electricity and Reductive CO2 Utilization. *Energy Environ. Sci.* **2020**, *13* (2), 472–494. https://doi.org/10.1039/C9EE02410G.

(3) Peplow, M. The Race to Upcycle CO2 into Fuels, Concrete and More. *Nature* **2022**, *603* (7903), 780–783. https://doi.org/10.1038/d41586-022-00807-y.

(4) Bushuyev, O. S.; De Luna, P.; Dinh, C. T.; Tao, L.; Saur, G.; van de Lagemaat, J.; Kelley, S. O.; Sargent, E. H. What Should We Make with CO2 and How Can We Make It? *Joule* **2018**, *2* (5), 825–832. https://doi.org/10.1016/j.joule.2017.09.003.

(5) Gao, W.; Liang, S.; Wang, R.; Jiang, Q.; Zhang, Y.; Zheng, Q.; Xie, B.; Toe, C. Y.; Zhu, X.; Wang, J.; Huang, L.; Gao, Y.; Wang, Z.; Jo, C.; Wang, Q.; Wang, L.; Liu, Y.; Louis, B.; Scott, J.; Roger, A.-C.; Amal, R.; He, H.; Park, S.-E. Industrial Carbon Dioxide Capture and Utilization: State of the Art and Future Challenges. *Chem. Soc. Rev.* **2020**, *49* (23), 8584–8686. https://doi.org/10.1039/D0CS00025F.

(6) Stephens, I. E. L.; Chan, K.; Bagger, A.; Boettcher, S. W.; Bonin, J.; Boutin, E.; Buckley, A. K.; Buonsanti, R.; Cave, E. R.; Chang, X.; Chee, S. W.; Silva, A. H. M. da; Luna, P. de; Einsle, O.; Endrődi, B.; Escudero-Escribano, M.; Araujo, J. V. F. de; Figueiredo, M. C.; Hahn, C.; Hansen, K. U.; Haussener, S.; Hunegnaw, S.; Huo, Z.; Hwang, Y. J.; Janáky, C.; Jayathilake, B. S.; Jiao, F.; Jovanov, Z. P.; Karimi, P.; Koper, M. T. M.; Kuhl, K. P.; Lee, W. H.; Liang, Z.; Liu, X.; Ma, S.; Ma, M.; Oh, H.-S.; Robert, M.; Cuenya, B. R.; Rossmeisl, J.; Roy, C.; Ryan, M. P.; Sargent, E. H.; Sebastián-Pascual, P.; Seger, B.; Steier, L.; Strasser, P.; Varela, A. S.; Vos, R. E.; Wang, X.; Xu, B.; Yadegari, H.; Zhou,

Y. 2022 Roadmap on Low Temperature Electrochemical CO2 Reduction. *J. Phys. Energy* **2022**, *4* (4), 042003. https://doi.org/10.1088/2515-7655/ac7823.

(7) Luna, P. D.; Hahn, C.; Higgins, D.; Jaffer, S. A.; Jaramillo, T. F.; Sargent, E. H. What Would It Take for Renewably Powered Electrosynthesis to Displace Petrochemical Processes? *Science* **2019**, *364* (6438), eaav3506. https://doi.org/10.1126/science.aav3506.

(8) P. Kuhl, K.; R. Cave, E.; N. Abram, D.; F. Jaramillo, T. New Insights into the Electrochemical Reduction of Carbon Dioxide on Metallic Copper Surfaces. *Energy & Environmental Science* **2012**, *5* (5), 7050–7059. https://doi.org/10.1039/C2EE21234J.

(9) Nitopi, S.; Bertheussen, E.; Scott, S. B.; Liu, X.; Engstfeld, A. K.; Horch, S.; Seger, B.; Stephens, I. E. L.; Chan, K.; Hahn, C.; Nørskov, J. K.; Jaramillo, T. F.; Chorkendorff, I. Progress and Perspectives of Electrochemical CO2 Reduction on Copper in Aqueous Electrolyte. *Chem. Rev.* **2019**, *119* (12), 7610–7672. https://doi.org/10.1021/acs.chemrev.8b00705.

(10) Ma, W.; He, X.; Wang, W.; Xie, S.; Zhang, Q.; Wang, Y. Electrocatalytic Reduction of CO 2 and CO to Multi-Carbon Compounds over Cu-Based Catalysts. *Chemical Society Reviews* **2021**, *50* (23), 12897–12914. https://doi.org/10.1039/D1CS00535A.

(11) Dinh, C.-T.; Burdyny, T.; Kibria, M. G.; Seifitokaldani, A.; Gabardo, C. M.; Arquer, F. P. G. de; Kiani, A.; Edwards, J. P.; Luna, P. D.; Bushuyev, O. S.; Zou, C.; Quintero-Bermudez, R.; Pang, Y.; Sinton, D.; Sargent, E. H. CO2 Electroreduction to Ethylene via Hydroxide-Mediated Copper Catalysis at an Abrupt Interface. *Science* **2018**, *360* (6390), 783–787. https://doi.org/10.1126/science.aas9100.

(12) Hoang, T. T. H.; Verma, S.; Ma, S.; Fister, T. T.; Timoshenko, J.; Frenkel, A. I.; Kenis, P. J. A.; Gewirth, A. A. Nanoporous Copper–Silver Alloys by Additive-Controlled Electrodeposition for the Selective Electroreduction of CO2 to Ethylene and Ethanol. *J. Am. Chem. Soc.* **2018**. https://doi.org/10.1021/jacs.8b01868.

(13) Choi, C.; Kwon, S.; Cheng, T.; Xu, M.; Tieu, P.; Lee, C.; Cai, J.; Lee, H. M.; Pan, X.; Duan, X.; Goddard, W. A.; Huang, Y. Highly Active and Stable Stepped Cu Surface for Enhanced Electrochemical CO 2 Reduction to C 2 H 4. *Nature Catalysis* **2020**, 1–9. https://doi.org/10.1038/s41929-020-00504-x.

(14) Li, Y.; Cui, F.; Ross, M. B.; Kim, D.; Sun, Y.; Yang, P. Structure-Sensitive CO2 Electroreduction to Hydrocarbons on Ultrathin 5-Fold Twinned Copper Nanowires. *Nano Lett.* **2017**, *17* (2), 1312–1317. https://doi.org/10.1021/acs.nanolett.6b05287.

(15) Weng, Z.; Wu, Y.; Wang, M.; Jiang, J.; Yang, K.; Huo, S.; Wang, X.-F.; Ma, Q.; Brudvig, G. W.; Batista, V. S.; Liang, Y.; Feng, Z.; Wang, H. Active Sites of Copper-Complex Catalytic Materials for Electrochemical Carbon Dioxide Reduction. *Nat Commun* **2018**, *9* (1), 415. https://doi.org/10.1038/s41467-018-02819-7.

(16) Hu, Q.; Han, Z.; Wang, X.; Li, G.; Wang, Z.; Huang, X.; Yang, H.; Ren, X.; Zhang, Q.; Liu, J.; He, C. Facile Synthesis of Sub-Nanometric Copper Clusters by Double Confinement Enables Selective Reduction of Carbon Dioxide to Methane. *Angewandte Chemie International Edition* **2020**, *59* (43), 19054–19059. https://doi.org/10.1002/anie.202009277.

(17) Karapinar, D.; Creissen, C. E.; Rivera de la Cruz, J. G.; Schreiber, M. W.; Fontecave, M. Electrochemical CO2 Reduction to Ethanol with Copper-Based Catalysts. *ACS Energy Lett.* **2021**, *6* (2), 694–706. https://doi.org/10.1021/acsenergylett.0c02610.

(18) Dry, M. E. The Fischer–Tropsch Process: 1950–2000. *Catalysis Today* **2002**, *71* (3–4), 227–241. https://doi.org/10.1016/S0920-5861(01)00453-9.

(19) Hernández, S.; Farkhondehfal, M. A.; Sastre, F.; Makkee, M.; Saracco, G.; Russo, N. Syngas Production from Electrochemical Reduction of CO 2 : Current Status and Prospective Implementation. *Green Chemistry* **2017**, *19* (10), 2326–2346. https://doi.org/10.1039/C7GC00398F.

(20) Peng, J.-B.; Geng, H.-Q.; Wu, X.-F. The Chemistry of CO: Carbonylation. *Chem* **2019**, *5* (3), 526–552. https://doi.org/10.1016/j.chempr.2018.11.006.

(21) Jouny, M.; Hutchings, G. S.; Jiao, F. Carbon Monoxide Electroreduction as an Emerging Platform for Carbon Utilization. *Nat Catal* **2019**, *2* (12), 1062–1070. https://doi.org/10.1038/s41929-019-0388-2.

(22) Ji, Y.; Guan, A.; Zheng, G. Copper-Based Catalysts for Electrochemical Carbon Monoxide Reduction. *Cell Reports Physical Science* **2022**, *3* (10), 101072. https://doi.org/10.1016/j.xcrp.2022.101072.
(23) Jouny, M.; Luc, W.; Jiao, F. High-Rate Electroreduction of Carbon Monoxide to Multi-Carbon Products. *Nat Catal* **2018**, *1* (10), 748–755. https://doi.org/10.1038/s41929-018-0133-2.
(24) Zhang, B.; Wang, L.; Li, D.; Li, Z.; Bu, R.; Lu, Y. Tandem Strategy for Electrochemical CO2 Reduction Reaction. *Chem Catalysis* **2022**, *2* (12), 3395–3429. https://doi.org/10.1016/j.checat.2022.10.017.
(25) S. Cousins, L.; E. Creissen, C. Multiscale Effects in Tandem CO 2 Electrolysis to C 2+ Products. *Nanoscale* **2024**. https://doi.org/10.1039/D3NR05547G.
(26) Somoza-Tornos, A.; Guerra, O. J.; Crow, A. M.; Smith, W. A.; Hodge, B.-M. Process Modeling, Techno-Economic Assessment, and Life Cycle Assessment of the Electrochemical Reduction of CO2: A Review. *iScience* **2021**, *24* (7), 102813. https://doi.org/10.1016/j.isci.2021.102813.
(27) Bonin, J.; Maurin, A.; Robert, M. Molecular Catalysis of the Electrochemical and Photochemical Reduction of CO2 with Fe and Co Metal Based Complexes. Recent Advances. *Coordination Chemistry Reviews* **2017**, *334*, 184–198. https://doi.org/10.1016/j.ccr.2016.09.005.
(28) Francke, R.; Schille, B.; Roemelt, M. Homogeneously Catalyzed Electroreduction of Carbon Dioxide—Methods, Mechanisms, and Catalysts. *Chem. Rev.* **2018**, *118* (9), 4631–4701. https://doi.org/10.1021/acs.chemrev.7b00459.
(29) Kinzel, N. W.; Werlé, C.; Leitner, W. Transition Metal Complexes as Catalysts for the Electroconversion of CO2: An Organometallic Perspective. *Angewandte Chemie International Edition* **2021**, *60* (21), 11628–11686. https://doi.org/10.1002/anie.202006988.
(30) Roy, S.; Sharma, B.; Pécaut, J.; Simon, P.; Fontecave, M.; Tran, P. D.; Derat, E.; Artero, V. Molecular Cobalt Complexes with Pendant Amines for Selective Electrocatalytic Reduction of Carbon Dioxide to Formic Acid. *J. Am. Chem. Soc.* **2017**, *139* (10), 3685–3696. https://doi.org/10.1021/jacs.6b11474.
(31) Franco Federico; Pinto Mara F.; Royo Beatriz; Lloret-Fillol Julio. A Highly Active N-Heterocyclic Carbene Manganese(I) Complex for Selective Electrocatalytic CO2 Reduction to CO. *Angewandte Chemie International Edition* **2018**, *57* (17), 4603–4606. https://doi.org/10.1002/anie.201800705.
(32) Su, X.; McCardle, K. M.; Chen, L.; Panetier, J. A.; Jurss, J. W. Robust and Selective Cobalt Catalysts Bearing Redox-Active Bipyridyl-N-Heterocyclic Carbene Frameworks for Electrochemical CO2 Reduction in Aqueous Solutions. *ACS Catal.* **2019**, 7398–7408. https://doi.org/10.1021/acscatal.9b00708.
(33) Sampson, M. D.; Nguyen, A. D.; Grice, K. A.; Moore, C. E.; Rheingold, A. L.; Kubiak, C. P. Manganese Catalysts with Bulky Bipyridine Ligands for the Electrocatalytic Reduction of Carbon Dioxide: Eliminating Dimerization and Altering Catalysis. *J. Am. Chem. Soc.* **2014**, *136* (14), 5460–5471. https://doi.org/10.1021/ja501252f.
(34) Nie, W.; Wang, Y.; Zheng, T.; Ibrahim, A.; Xu, Z.; McCrory, C. C. L. Electrocatalytic CO2 Reduction by Cobalt Bis(Pyridylmonoimine) Complexes: Effect of Ligand Flexibility on Catalytic Activity. *ACS Catal.* **2020**, *10* (9), 4942–4959. https://doi.org/10.1021/acscatal.9b05513.
(35) Chatterjee, B.; Chang, W.-C.; Werlé, C. Molecularly Controlled Catalysis – Targeting Synergies Between Local and Non-Local Environments. *ChemCatChem* **2021**, *13* (7), 1659–1682. https://doi.org/10.1002/cctc.202001431.
(36) Queyriaux, N. Redox-Active Ligands in Electroassisted Catalytic H+ and CO2 Reductions: Benefits and Risks. *ACS Catal.* **2021**, *11* (7), 4024–4035. https://doi.org/10.1021/acscatal.1c00237.
(37) Nie, W.; Tarnopol, D. E.; McCrory, C. C. L. Enhancing a Molecular Electrocatalyst's Activity for CO2 Reduction by Simultaneously Modulating Three Substituent Effects. *J. Am. Chem. Soc.* **2021**, *143* (10), 3764–3778. https://doi.org/10.1021/jacs.0c09357.
(38) Ginovska-Pangovska, B.; Dutta, A.; Reback, M. L.; Linehan, J. C.; Shaw, W. J. Beyond the Active Site: The Impact of the Outer Coordination Sphere on Electrocatalysts for Hydrogen Production and Oxidation. *Acc. Chem. Res.* **2014**, *47* (8), 2621–2630. https://doi.org/10.1021/ar5001742.

(39) Azcarate, I.; Costentin, C.; Robert, M.; Savéant, J.-M. Through-Space Charge Interaction Substituent Effects in Molecular Catalysis Leading to the Design of the Most Efficient Catalyst of CO2-to-CO Electrochemical Conversion. *J. Am. Chem. Soc.* **2016**, *138* (51), 16639–16644. https://doi.org/10.1021/jacs.6b07014.
(40) Nichols, A. W.; Machan, C. W. Secondary-Sphere Effects in Molecular Electrocatalytic CO2 Reduction. *Front. Chem.* **2019**, *7* (397), 1–19. https://doi.org/10.3389/fchem.2019.00397.
(41) Gotico, P.; Boitrel, B.; Guillot, R.; Sircoglou, M.; Quaranta, A.; Halime, Z.; Leibl, W.; Aukauloo, A. Second-Sphere Biomimetic Multipoint Hydrogen-Bonding Patterns to Boost CO2 Reduction of Iron Porphyrins. *Angewandte Chemie International Edition* **2019**, *58* (14), 4504–4509. https://doi.org/10.1002/anie.201814339.
(42) Léonard, N. G.; Dhaoui, R.; Chantarojsiri, T.; Yang, J. Y. Electric Fields in Catalysis: From Enzymes to Molecular Catalysts. *ACS Catal.* **2021**, *11* (17), 10923–10932. https://doi.org/10.1021/acscatal.1c02084.
(43) Jakobsen, J. B.; Rønne, M. H.; Daasbjerg, K.; Skrydstrup, T. Are Amines the Holy Grail for Facilitating CO2 Reduction? *Angewandte Chemie International Edition* **2021**, *60* (17), 9174–9179. https://doi.org/10.1002/anie.202014255.
(44) Drover, M. W. A Guide to Secondary Coordination Sphere Editing. *Chem. Soc. Rev.* **2022**, *51* (6), 1861–1880. https://doi.org/10.1039/D2CS00022A.
(45) Bullock, R. M.; Das, A. K.; Appel, A. M. Surface Immobilization of Molecular Electrocatalysts for Energy Conversion. *Chem. Eur. J.* **2017**, *23* (32), 7626–7641. https://doi.org/10.1002/chem.201605066.
(46) Dalle, K. E.; Warnan, J.; Leung, J. J.; Reuillard, B.; Karmel, I. S.; Reisner, E. Electro- and Solar-Driven Fuel Synthesis with First Row Transition Metal Complexes. *Chem. Rev.* **2019**, *119* (4), 2752–2875. https://doi.org/10.1021/acs.chemrev.8b00392.
(47) Sun, L.; Reddu, V.; Fisher, A. C.; Wang, X. Electrocatalytic Reduction of Carbon Dioxide: Opportunities with Heterogeneous Molecular Catalysts. *Energy Environ. Sci.* **2020**, *13* (2), 374–403. https://doi.org/10.1039/C9EE03660A.
(48) Lv, F.; Han, N.; Qiu, Y.; Liu, X.; Luo, J.; Li, Y. Transition Metal Macrocycles for Heterogeneous Electrochemical CO2 Reduction. *Coordination Chemistry Reviews* **2020**, *422*, 213435. https://doi.org/10.1016/j.ccr.2020.213435.
(49) Wu, Y.; Liang, Y.; Wang, H. Heterogeneous Molecular Catalysts of Metal Phthalocyanines for Electrochemical CO2 Reduction Reactions. *Acc. Chem. Res.* **2021**, *54* (16), 3149–3159. https://doi.org/10.1021/acs.accounts.1c00200.
(50) Maurin, A.; Robert, M. Noncovalent Immobilization of a Molecular Iron-Based Electrocatalyst on Carbon Electrodes for Selective, Efficient CO2-to-CO Conversion in Water. *J. Am. Chem. Soc.* **2016**, *138* (8), 2492–2495. https://doi.org/10.1021/jacs.5b12652.
(51) Boutin, E.; Merakeb, L.; Ma, B.; Boudy, B.; Wang, M.; Bonin, J.; Anxolabéhère-Mallart, E.; Robert, M. Molecular Catalysis of CO2 Reduction: Recent Advances and Perspectives in Electrochemical and Light-Driven Processes with Selected Fe, Ni and Co Aza Macrocyclic and Polypyridine Complexes. *Chem. Soc. Rev.* **2020**, *49* (16), 5772–5809. https://doi.org/10.1039/D0CS00218F.
(52) Zhang, X.; Wang, Y.; Gu, M.; Wang, M.; Zhang, Z.; Pan, W.; Jiang, Z.; Zheng, H.; Lucero, M.; Wang, H.; Sterbinsky, G. E.; Ma, Q.; Wang, Y.-G.; Feng, Z.; Li, J.; Dai, H.; Liang, Y. Molecular Engineering of Dispersed Nickel Phthalocyanines on Carbon Nanotubes for Selective CO 2 Reduction. *Nature Energy* **2020**, *5* (9), 684–692. https://doi.org/10.1038/s41560-020-0667-9.
(53) Hu, X.-M.; Rønne, M. H.; Pedersen, S. U.; Skrydstrup, T.; Daasbjerg, K. Enhanced Catalytic Activity of Cobalt Porphyrin in CO2 Electroreduction upon Immobilization on Carbon Materials. *Angewandte Chemie International Edition* **2017**, *56* (23), 6468–6472. https://doi.org/10.1002/anie.201701104.
(54) Sinha, S.; Zhang, R.; Warren, J. J. Low Overpotential CO2 Activation by a Graphite-Adsorbed Cobalt Porphyrin. *ACS Catal.* **2020**, 12284–12291. https://doi.org/10.1021/acscatal.0c01367.
(55) Pugliese, S.; Huan, N. T.; Solé-Daura, A.; Li, Y.; Rivera de la Cruz, J.-G.; Forte, J.; Zanna, S.; Krief, A.; Su, B.-L.; Fontecave, M. CO2 Electroreduction in Water with a Heterogenized C-Substituted

Nickel Cyclam Catalyst. *Inorg. Chem.* **2022**, *61* (40), 15841–15852. https://doi.org/10.1021/acs.inorgchem.2c01645.

(56) Elgrishi, N.; Griveau, S.; Chambers, M. B.; Bedioui, F.; Fontecave, M. Versatile Functionalization of Carbon Electrodes with a Polypyridine Ligand: Metallation and Electrocatalytic H+ and CO2 Reduction. *Chem. Commun.* **2015**, *51* (14), 2995–2998. https://doi.org/10.1039/C4CC10027A.

(57) Sun Cunfa; Rotundo Laura; Garino Claudio; Nencini Luca; Yoon Sam S.; Gobetto Roberto; Nervi Carlo. Electrochemical CO2 Reduction at Glassy Carbon Electrodes Functionalized by MnI and ReI Organometallic Complexes. *ChemPhysChem* **2017**, *18* (22), 3219–3229. https://doi.org/10.1002/cphc.201700739.

(58) Reuillard, B.; Ly, K. H.; Rosser, T. E.; Kuehnel, M. F.; Zebger, I.; Reisner, E. Tuning Product Selectivity for Aqueous CO2 Reduction with a Mn(Bipyridine)-Pyrene Catalyst Immobilized on a Carbon Nanotube Electrode. *J. Am. Chem. Soc.* **2017**, *139* (41), 14425–14435. https://doi.org/10.1021/jacs.7b06269.

(59) Wang, M.; Chen, L.; Lau, T.-C.; Robert, M. A Hybrid Co Quaterpyridine Complex/Carbon Nanotube Catalytic Material for CO2 Reduction in Water. *Angewandte Chemie International Edition* **2018**, *57* (26), 7769–7773. https://doi.org/10.1002/anie.201802792.

(60) Leung, J. J.; Vigil, J. A.; Warnan, J.; Edwardes Moore, E.; Reisner, E. Rational Design of Polymers for Selective CO2 Reduction Catalysis. *Angewandte Chemie International Edition* **2019**, *58* (23), 7697–7701. https://doi.org/10.1002/anie.201902218.

(61) Wu, Y.; Jiang, Z.; Lu, X.; Liang, Y.; Wang, H. Domino Electroreduction of CO 2 to Methanol on a Molecular Catalyst. *Nature* **2019**, *575* (7784), 639–642. https://doi.org/10.1038/s41586-019-1760-8.

(62) Su, J.; Zhang, J.-J.; Chen, J.; Song, Y.; Huang, L.; Zhu, M.; Yakobson, B. I.; Tang, B. Z.; Ye, R. Building a Stable Cationic Molecule/Electrode Interface for Highly Efficient and Durable CO2 Reduction at an Industrially Relevant Current. *Energy Environ. Sci.* **2021**, *14* (1), 483–492. https://doi.org/10.1039/D0EE02535F.

(63) Matheu, R.; Gutierrez-Puebla, E.; Monge, M. Á.; Diercks, C. S.; Kang, J.; Prévot, M. S.; Pei, X.; Hanikel, N.; Zhang, B.; Yang, P.; Yaghi, O. M. Three-Dimensional Phthalocyanine Metal-Catecholates for High Electrochemical Carbon Dioxide Reduction. *J. Am. Chem. Soc.* **2019**, *141* (43), 17081–17085. https://doi.org/10.1021/jacs.9b09298.

(64) Dubed Bandomo, G. C.; Mondal, S. S.; Franco, F.; Bucci, A.; Martin-Diaconescu, V.; Ortuño, M. A.; van Langevelde, P. H.; Shafir, A.; López, N.; Lloret-Fillol, J. Mechanically Constrained Catalytic Mn(CO)3Br Single Sites in a Two-Dimensional Covalent Organic Framework for CO2 Electroreduction in H2O. *ACS Catal.* **2021**, 7210–7222. https://doi.org/10.1021/acscatal.1c00314.

(65) Zhou, Y.; Liu, S.; Gu, Y.; Wen, G.-H.; Ma, J.; Zuo, J.-L.; Ding, M. In(III) Metal–Organic Framework Incorporated with Enzyme-Mimicking Nickel Bis(Dithiolene) Ligand for Highly Selective CO2 Electroreduction. *J. Am. Chem. Soc.* **2021**. https://doi.org/10.1021/jacs.1c06797.

(66) Torbensen, K.; Boudy, B.; Joulié, D.; von Wolff, N.; Robert, M. Emergence of CO2 Electrolyzers Including Supported Molecular Catalysts. *Current Opinion in Electrochemistry* **2020**, *24*, 49–55. https://doi.org/10.1016/j.coelec.2020.07.001.

(67) Ren, S.; Joulié, D.; Salvatore, D.; Torbensen, K.; Wang, M.; Robert, M.; Berlinguette, C. P. Molecular Electrocatalysts Can Mediate Fast, Selective CO2 Reduction in a Flow Cell. *Science* **2019**, *365* (6451), 367–369. https://doi.org/10.1126/science.aax4608.

(68) Siritanaratkul, B.; Forster, M.; Greenwell, F.; Sharma, P. K.; Yu, E. H.; Cowan, A. J. Zero-Gap Bipolar Membrane Electrolyzer for Carbon Dioxide Reduction Using Acid-Tolerant Molecular Electrocatalysts. *J. Am. Chem. Soc.* **2022**, *144* (17), 7551–7556. https://doi.org/10.1021/jacs.1c13024.

(69) Ren, S.; Lees, E. W.; Hunt, C.; Jewlal, A.; Kim, Y.; Zhang, Z.; Mowbray, B. A. W.; Fink, A. G.; Melo, L.; Grant, E. R.; Berlinguette, C. P. Catalyst Aggregation Matters for Immobilized Molecular CO2RR Electrocatalysts. *J. Am. Chem. Soc.* **2023**, *145* (8), 4414–4420. https://doi.org/10.1021/jacs.2c08380.

(70) Lacy, D. C.; McCrory, C. C. L.; Peters, J. C. Studies of Cobalt-Mediated Electrocatalytic CO2 Reduction Using a Redox-Active Ligand. *Inorg. Chem.* **2014**, *53* (10), 4980–4988. https://doi.org/10.1021/ic403122j.
(71) Zhang, M.; El-Roz, M.; Frei, H.; Mendoza-Cortes, J. L.; Head-Gordon, M.; Lacy, D. C.; Peters, J. C. Visible Light Sensitized CO2 Activation by the Tetraaza [CoIIN4H(MeCN)]2+ Complex Investigated by FT-IR Spectroscopy and DFT Calculations. *J. Phys. Chem. C* **2015**, *119* (9), 4645–4654. https://doi.org/10.1021/jp5127738.
(72) Sheng, H.; Frei, H. Direct Observation by Rapid-Scan FT-IR Spectroscopy of Two-Electron-Reduced Intermediate of Tetraaza Catalyst [CoIIN4H(MeCN)]2+ Converting CO2 to CO. *J. Am. Chem. Soc.* **2016**, *138* (31), 9959–9967. https://doi.org/10.1021/jacs.6b05248.
(73) Nguyen, D. N.; Giannoudis, E.; Straistari, T.; Fize, J.; Koepf, M.; Tran, P. D.; Chavarot-Kerlidou, M.; Artero, V. Unassisted Solar Syngas Production by a Molecular Dye-Cobalt Catalyst Assembly in a Tandem Photoelectrochemical Cell. *ACS Energy Lett.* **2024**, *9* (3), 829–834. https://doi.org/10.1021/acsenergylett.3c02480.
(74) Johnson, B. A.; Beiler, A. M.; McCarthy, B. D.; Ott, S. Transport Phenomena: Challenges and Opportunities for Molecular Catalysis in Metal–Organic Frameworks. *J. Am. Chem. Soc.* **2020**, *142* (28), 11941–11956. https://doi.org/10.1021/jacs.0c02899.
(75) Schild, J.; Reuillard, B.; Morozan, A.; Chenevier, P.; Gravel, E.; Doris, E.; Artero, V. Approaching Industrially Relevant Current Densities for Hydrogen Oxidation with a Bioinspired Molecular Catalytic Material. *J. Am. Chem. Soc.* **2021**, *143* (43), 18150–18158. https://doi.org/10.1021/jacs.1c07093.
(76) Moonshiram, D.; Gimbert-Suriñach, C.; Guda, A.; Picon, A.; Lehmann, C. S.; Zhang, X.; Doumy, G.; March, A. M.; Benet-Buchholz, J.; Soldatov, A.; Llobet, A.; Southworth, S. H. Tracking the Structural and Electronic Configurations of a Cobalt Proton Reduction Catalyst in Water. *J. Am. Chem. Soc.* **2016**, *138* (33), 10586–10596. https://doi.org/10.1021/jacs.6b05680.
(77) DeLuca, E. E.; Chan, T.; Taylor, J. M.; Lee, B.; Prabhakar, R. R.; Kubiak, C. P. Steric Effects on CO2 Reduction with Substituted Mn(Bpy)(CO)3X-Type Catalysts on Multiwalled Carbon Nanotubes Reveal Critical Mechanistic Details. *ACS Catal.* **2024**, *14* (3), 2071–2083. https://doi.org/10.1021/acscatal.3c05771.
(78) Chan, T.; Zoric, M. R.; Shandilya, A.; Loeb, C. K.; Barrett, J. A.; Cordones, A. A.; Kubiak, C. P. Simple Preparation and Characterization of Hybrid Cobalt Phthalocyanine on Multiwalled Carbon Nanotube Electrodes. *ACS Appl. Energy Mater.* **2024**, *7* (6), 2225–2233. https://doi.org/10.1021/acsaem.3c02953.
(79) Shang, B.; Zhao, F.; Suo, S.; Gao, Y.; Sheehan, C.; Jeon, S.; Li, J.; Rooney, C. L.; Leitner, O.; Xiao, L.; Fan, H.; Elimelech, M.; Wang, L.; Meyer, G. J.; Stach, E. A.; Mallouk, T. E.; Lian, T.; Wang, H. Tailoring Interfaces for Enhanced Methanol Production from Photoelectrochemical CO2 Reduction. *J. Am. Chem. Soc.* **2024**, *146* (3), 2267–2274. https://doi.org/10.1021/jacs.3c13540.
(80) Reuillard, B.; Goff, A. L.; Cosnier, S. Non-Covalent Double Functionalization of Carbon Nanotubes with a NADH Oxidation Ru(II)-Based Molecular Catalyst and a NAD-Dependent Glucose Dehydrogenase. *Chem. Commun.* **2014**, *50* (79), 11731–11734. https://doi.org/10.1039/C4CC04758C.
(81) Kaminsky, C. J.; Weng, S.; Wright, J.; Surendranath, Y. Adsorbed Cobalt Porphyrins Act like Metal Surfaces in Electrocatalysis. *Nat Catal* **2022**, *5* (5), 430–442. https://doi.org/10.1038/s41929-022-00791-6.
(82) Laviron, E. General Expression of the Linear Potential Sweep Voltammogram in the Case of Diffusionless Electrochemical Systems. *Journal of Electroanalytical Chemistry and Interfacial Electrochemistry* **1979**, *101* (1), 19–28. https://doi.org/10.1016/S0022-0728(79)80075-3.
(83) Hanna, C. M.; Sanborn, C. D.; Ardo, S.; Yang, J. Y. Interfacial Electron Transfer of Ferrocene Immobilized onto Indium Tin Oxide through Covalent and Noncovalent Interactions. *ACS Appl. Mater. Interfaces* **2018**, *10* (15), 13211–13217. https://doi.org/10.1021/acsami.8b01219.
(84) Bagnall, A. J.; Haake, M.; Grau, S.; Straistari, T.; Koepf, M.; Jameei Moghaddam, N.; Gimbert-Suriñach, C.; Benet-Buchholz, J.; Llobet, A.; Chavarot-Kerlidou, M.; Reuillard, B.; Artero, V.

Molecular Engineering of Electrocatalytic Nanomaterials for Hydrogen Evolution: The Impact of Structural and Electronic Modifications of Anchoring Linkers on Electrocatalysis. *ACS Catal.* **2024**, *14* (8), 5630–5638. https://doi.org/10.1021/acscatal.4c00336.

(85) Dhar, D.; McKenas, C. G.; Huang, C.-W.; Atkin, J. M.; Dempsey, J. L.; Lockett, M. R. Quantitative Effects of Disorder on Chemically Modified Amorphous Carbon Electrodes. *ACS Appl. Energy Mater.* **2020**, *3* (8), 8038–8047. https://doi.org/10.1021/acsaem.0c01434.

(86) Blanchard, P.-Y.; Alévêque, O.; Boisard, S.; Gautier, C.; El-Ghayoury, A.; Derf, F. L.; Breton, T.; Levillain, E. Intermolecular Interactions in Self-Assembled Monolayers of Tetrathiafulvalene Derivatives. *Physical Chemistry Chemical Physics* **2011**, *13* (6), 2118–2120. https://doi.org/10.1039/C0CP01968B.

(87) Alévêque, O.; Levillain, E. A Generalized Lateral Interactions Function to Fit Voltammetric Peaks of Self-Assembled Monolayers. *Electrochemistry Communications* **2016**, *67*, 73–79. https://doi.org/10.1016/j.elecom.2016.04.003.

(88) Sosna, M.; Ferapontova, E. E. Electron Transfer in Binary Hemin-Modified Alkanethiol Self-Assembled Monolayers on Gold: Hemin's Lateral and Interfacial Interactions. *Langmuir* **2022**, *38* (37), 11180–11190. https://doi.org/10.1021/acs.langmuir.2c01064.

(89) Zhanaidarova, A.; Jones, S. C.; Despagnet-Ayoub, E.; Pimentel, B. R.; Kubiak, C. P. Re(TBu-Bpy)(CO)3Cl Supported on Multi-Walled Carbon Nanotubes Selectively Reduces CO2 in Water. *J. Am. Chem. Soc.* **2019**, *141* (43), 17270–17277. https://doi.org/10.1021/jacs.9b08445.

(90) Wu, Y.; Hu, G.; Rooney, C. L.; Brudvig, G. W.; Wang, H. Heterogeneous Nature of Electrocatalytic CO/CO2 Reduction by Cobalt Phthalocyanines. *ChemSusChem* **2020**, *13* (23), 6296–6299. https://doi.org/10.1002/cssc.202001396.

(91) Wiedner, E. S.; Chambers, M. B.; Pitman, C. L.; Bullock, R. M.; Miller, A. J. M.; Appel, A. M. Thermodynamic Hydricity of Transition Metal Hydrides. *Chem. Rev.* **2016**, *116* (15), 8655–8692. https://doi.org/10.1021/acs.chemrev.6b00168.

(92) Wagner, A.; Sahm, C. D.; Reisner, E. Towards Molecular Understanding of Local Chemical Environment Effects in Electro- and Photocatalytic CO 2 Reduction. *Nature Catalysis* **2020**, *3* (10), 775–786. https://doi.org/10.1038/s41929-020-00512-x.

(93) Jackson, M. N.; Oh, S.; Kaminsky, C. J.; Chu, S. B.; Zhang, G.; Miller, J. T.; Surendranath, Y. Strong Electronic Coupling of Molecular Sites to Graphitic Electrodes via Pyrazine Conjugation. *J. Am. Chem. Soc.* **2018**, *140* (3), 1004–1010. https://doi.org/10.1021/jacs.7b10723.

(94) Jackson, M. N.; Kaminsky, C. J.; Oh, S.; Melville, J. F.; Surendranath, Y. Graphite Conjugation Eliminates Redox Intermediates in Molecular Electrocatalysis. *J. Am. Chem. Soc.* **2019**. https://doi.org/10.1021/jacs.9b04981.

(95) Edwardes Moore, E.; Cobb, S. J.; Coito, A. M.; Oliveira, A. R.; Pereira, I. A. C.; Reisner, E. Understanding the Local Chemical Environment of Bioelectrocatalysis. *Proceedings of the National Academy of Sciences* **2022**, *119* (4), e2114097119. https://doi.org/10.1073/pnas.2114097119.

(96) Andrin, B.; Junior, P. J. M. C.; Provost, D.; Diring, S.; Pellegrin, Y.; Robert, M.; Odobel, F. Carbon Nanotube Heterogenization Improves Cobalt Pyridyldiimine Complex CO2 Reduction Activity in Aqueous Carbonate Buffer. *Chem. Commun.* **2024**. https://doi.org/10.1039/D4CC00629A.

(97) Zamader, A.; Reuillard, B.; Marcasuzaa, P.; Bousquet, A.; Billon, L.; Espí Gallart, J. J.; Berggren, G.; Artero, V. Electrode Integration of Synthetic Hydrogenase as Bioinspired and Noble Metal-Free Cathodes for Hydrogen Evolution. *ACS Catal.* **2023**, *13* (2), 1246–1256. https://doi.org/10.1021/acscatal.2c05175.

(98) Zhu, M.; Ye, R.; Jin, K.; Lazouski, N.; Manthiram, K. Elucidating the Reactivity and Mechanism of CO2 Electroreduction at Highly Dispersed Cobalt Phthalocyanine. *ACS Energy Lett.* **2018**, *3* (6), 1381–1386. https://doi.org/10.1021/acsenergylett.8b00519.

(99) Soucy, T. L.; Liu, Y.; Eisenberg, J. B.; McCrory, C. C. L. Enhancing the Electrochemical CO2 Reduction Activity of Polymer-Encapsulated Cobalt Phthalocyanine Films by Modulating the Loading of Catalysts, Polymers, and Carbon Supports. *ACS Appl. Energy Mater.* **2022**, *5* (1), 159–169. https://doi.org/10.1021/acsaem.1c02689.